

# ReGNet: Reciprocal Space-Aware Long-Range Modeling for Crystalline Property Prediction

Jianan Nie<sup>\*†</sup> Peiyao Xiao<sup>\*‡</sup> Kaiyi Ji<sup>‡</sup> Peng Gao<sup>†</sup>

May 29, 2025

## Abstract

Predicting properties of crystals from their structures is a fundamental yet challenging task in materials science. Unlike molecules, crystal structures exhibit infinite periodic arrangements of atoms, requiring methods capable of capturing both local and global information effectively. However, most current works fall short of capturing long-range interactions within periodic structures. To address this limitation, we leverage *reciprocal space* to efficiently encode long-range interactions with learnable filters within Fourier transforms. We introduce Reciprocal Geometry Network (ReGNet), a novel architecture that integrates geometric GNNs and reciprocal blocks to model short-range and long-range interactions, respectively. Experimental results on JARVIS, Materials Project, and MatBench demonstrate that ReGNet achieves state-of-the-art predictive accuracy across a range of crystal property prediction tasks. Additionally, we explore a model extension that employs the mixture-of-experts for multi-property prediction with promising results and high computational efficiency. These findings highlight the potential of our model as a scalable and accurate solution for crystal property prediction. The code will be released upon paper acceptance.

## 1 Introduction

AI-driven methods for accelerated material property prediction (Choudhary et al., 2022) have achieved notable success in materials sciences. As the demand for novel materials grows, traditional methods like wet lab experiments are costly and time-intensive. Computational methods such as density functional theory (DFT) offer advances but remain limited by high computational costs, hindering scalable exploration of the vast materials space (Jones, 2015). To overcome these challenges, recent studies have adopted machine learning (ML) models in material property prediction and accelerating discovery (Chen et al., 2019; Yan et al., 2022; Zeni et al., 2023; Lin et al., 2023; Yan et al., 2024).

Crystals are solid materials extensively utilized across various scientific and industrial domains, including semiconductors, photonics, catalysis, and pharmaceuticals (Ashcroft & Mermin, 2001). Unlike molecules, crystal structures possess a unique and essential structural feature called *periodicity*, in which atoms are arranged in a highly ordered, infinitely repeating pattern that extends in three-dimensional (3D) space, as illustrated in Figure 1. This periodic arrangement, referred to as the crystal lattice, fundamentally shapes the material’s distinct physical and chemical properties. Recently, graph neural network (GNN)-based methods have been developed to predict these properties by constructing graphs connecting atoms within a *small*, pre-defined distance threshold (Xie & Grossman, 2018; Schütt et al., 2018; Chen et al., 2019; Louis et al., 2020; Choudhary & DeCost, 2021). However, these methods fail to explicitly capture long-range interactions between distant atoms.

A key challenge in predicting crystal properties is *effectively encoding long-range atomic interactions within periodic structures*. The previous GNN-based method, PotNet (Lin et al., 2023), uses fixed-form physical equations to

<sup>\*</sup>Equal contribution.

<sup>†</sup>Jianan Nie and Peng Gao are with Department of Computer Science, Virginia Tech, Blacksburg, VA, United States (e-mail: jianan@vt.edu, penggao@vt.edu).

<sup>‡</sup>Peiyao Xiao and Kaiyi Ji are with Department of Computer Science and Engineering, University at Buffalo, Buffalo, NY, United States (e-mail: peiyaoxi@buffalo.edu, kaiyiji@buffalo.edu).

compute infinite potential summations as edge features. However, this method incurs an additional  $\mathcal{O}(n^2)$  computational cost, making it inefficient for complex material systems with large  $n$ , where  $n$  is the number of atoms in the unit cell. Furthermore, material interactions are inherently complicated and cannot be adequately captured by a direct summation of a few predefined potentials.

In this work, we utilize *reciprocal space* to efficiently encode long-range interactions using learnable continuous filters with Fourier transforms in crystalline materials. Reciprocal space provides a mathematical framework to describe the periodic structure of crystals, enabling the analysis and prediction of material properties influenced by periodicity Economou (2010). While long-range interactions decay slowly with distance in real space, their Fourier transform decays rapidly, enabling efficient computations. Despite its fundamental importance, reciprocal space remains largely overlooked in crystal representation learning. Thus, integrating reciprocal space information into such models presents a novel opportunity to capture global periodicity and interactions, with the potential to substantially improve the accuracy of predictions.

Previous work, EwaldMP (Kosmala et al., 2023), encodes molecular long-range interactions using Fourier transforms, but only for molecular systems and relies on a predefined supercell grid size as hyperparameters, which can disrupt unit cell symmetry. In contrast, our method leverages reciprocal lattice vectors and atomic fractional coordinates, thus eliminating dependence on predefined supercell grids and enhancing symmetry preservation for more accurate modeling. Crystalformer (Taniai et al., 2024) introduces reciprocal space via fixed Fourier distance features to enable infinite range attention, where it is non-trainable and appears only as an optional variant in the appendix. In contrast, we utilize message passing with learnable continuous filters, parameterized by neural networks, to enable more precise representations of long-range interactions in complex crystals. In brief, this paper makes the following contributions.

- **Reciprocal space.** We introduce the first end-to-end framework that incorporates reciprocal space with trainable Fourier-space filters into message passing for crystalline materials, enabling reciprocal space informed modeling of long-range interactions.
- **Architecture design.** We introduce a new model, *Reciprocal Geometry Network (ReGNet)*. It consists of multiple message-passing blocks, where each block comprises a geometric GNN for short-range interactions and a novel reciprocal block for long-range interactions.
- **Superior empirical performance.** Extensive experiments show that ReGNet achieves state-of-the-art performance compared to various methods across common material property prediction datasets, JARVIS, the Material Project, and MatBench datasets.

## 2 Preliminary

### 2.1 Periodic Crystal Structure Representation

A crystalline material can be represented as the infinite periodic arrangement of atoms in 3D space, with the smallest repeating structural unit referred to as the unit cell. The unit cell defines the lattice symmetry and dictates the overall

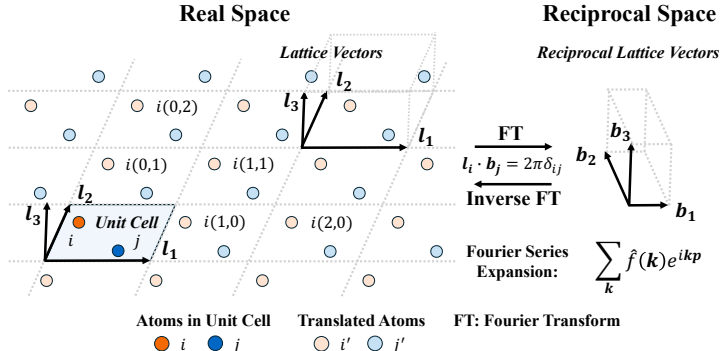


Figure 1: Illustration of the relationship between real space (left) and reciprocal space (right) in crystals. Long-range interactions can be computed through the Fourier series expansion. See Section 2.2 for details.

periodicity and physical properties of the material. The structure of crystals is commonly represented using two coordinate systems: the Cartesian coordinate system and the fractional coordinate system.

**Cartesian coordinate.** Mathematically, a material can be represented as  $\mathbf{M} = (\mathbf{A}, \mathbf{P}, \mathbf{L})$ .  $\mathbf{A} = [\mathbf{a}_1, \mathbf{a}_2, \dots, \mathbf{a}_n]^\top \in \mathbb{R}^{n \times h}$  denotes the atom feature matrix for  $n$  atoms within a unit cell, where  $\mathbf{a}_i \in \mathbb{R}^h$  represents the  $h$ -dimensional features of atom  $i$  in the unit cell.  $\mathbf{P} = [\mathbf{p}_1, \mathbf{p}_2, \dots, \mathbf{p}_n]^\top \in \mathbb{R}^{n \times 3}$  is the position matrix, where  $\mathbf{p}_i \in \mathbb{R}^3$  is the Cartesian coordinate of atom  $i$  inside the unit cell. In crystallography, a lattice is a periodic arrangement of points that defines a crystal’s translational symmetry. As shown in Figure 1, the lattice matrix  $\mathbf{L} = [\ell_1, \ell_2, \ell_3]^\top \in \mathbb{R}^{3 \times 3}$  consists of three translation lattice vectors that determine the shape and periodicity of the unit cell. The periodic repetition of the unit cell is described by integer multiples of the lattice vectors, ensuring translational invariance. Specifically, the infinite crystal structure can be expressed as:

$$\hat{\mathbf{P}} = \{\hat{\mathbf{p}}_i | \hat{\mathbf{p}}_i = \mathbf{p}_i + n_1 \ell_1 + n_2 \ell_2 + n_3 \ell_3, n_1, n_2, n_3 \in \mathbb{Z}, i \in \mathbb{Z}, 1 \leq i \leq n\}$$

where the integers  $n_1, n_2, n_3$  define a 3D translation with  $\ell_1, \ell_2, \ell_3$ .  $\hat{\mathbf{A}} = \{\hat{\mathbf{a}}_i | \hat{\mathbf{a}}_i = \mathbf{a}_i, i \in \mathbb{Z}, 1 \leq i \leq n\}$  is the atom feature in repeated unit cells, which remains unchanged under periodic translation.

**Fractional coordinate.** Fractional coordinates capture the relative positions of atoms within the unit cell and offer significant advantages for periodic materials compared to Cartesian coordinates. Specifically, the fractional coordinate uses the lattice matrix  $\mathbf{L} \in \mathbb{R}^{3 \times 3}$  as the basis, where atomic positions are described by fractional coordinate vectors  $\mathbf{f}_i = [f_1, f_2, f_3]^\top \in [0, 1)^3$ . The corresponding Cartesian coordinates are obtained as  $\mathbf{p}_i = \mathbf{L} \mathbf{f}_i$ , where  $\mathbf{p}_i = f_1 \ell_1 + f_2 \ell_2 + f_3 \ell_3$ . The representation of crystal  $\mathbf{M}$  generalizes to  $\mathbf{M} = (\mathbf{A}, \mathbf{F}, \mathbf{L})$ , where  $\mathbf{F} = [\mathbf{f}_1, \dots, \mathbf{f}_n]^\top \in [0, 1)^{n \times 3}$  denotes the fractional coordinates of all atoms in the unit cell. Fractional coordinates inherently align with lattice periodicity, ensuring that calculations respect periodic boundary conditions. Moreover, they remain invariant under space group operations, such as translations and rotations, thereby preserving structural relationships. These properties make fractional coordinates a more efficient and symmetry-aware representation for periodic materials compared to Cartesian coordinates.

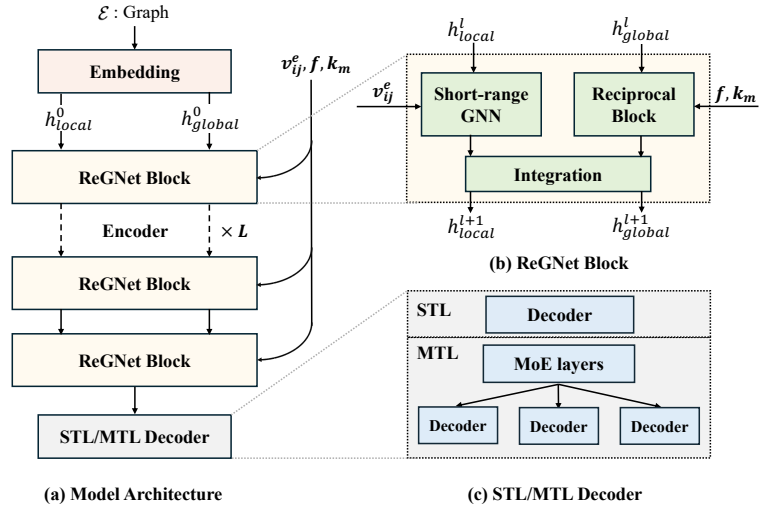


Figure 2: Overall framework architecture, consisting of three components: (a) Model architecture, (b) ReGNet block, and (c) Decoder. The model uses stacked ReGNet blocks, which integrate local features via message passing and global features via reciprocal space convolution. The decoder outputs property predictions for single-task and multi-task settings.

## 2.2 Reciprocal Space in Crystalline Materials

The periodic arrangement of atoms in crystalline materials fundamentally influences their physical properties by establishing a repeating structure that extends over long distances. Reciprocal space provides a mathematical framework to describe the periodic structure of crystals, enabling the analysis and prediction of material properties influenced by periodicity (Ashcroft & Mermin (2001); Gross & Marx (2014); Economou (2010)). Reciprocal space consists of wave

vectors  $\mathbf{k}$  spanned by reciprocal lattice vectors  $\mathbf{b}_1, \mathbf{b}_2, \mathbf{b}_3$ , which are derived from lattice vectors in real space  $\ell_1, \ell_2, \ell_3$ , with relationship satisfying  $\mathbf{b}_i \cdot \ell_j = 2\pi\delta_{ij}$ , where  $\delta_{ij}$  is the Kronecker delta. Each vector in reciprocal space represents a spatial frequency that encodes crystal periodicity along specific directions. More details can be found in Appendix A.

To establish the reciprocal space representation, we employ the Fourier transform, which expresses the periodic function  $f$  via Fourier series expansion:

$$f(\mathbf{p}_j) = \sum_{\mathbf{k}} \hat{f}(\mathbf{k}) \exp(i\mathbf{k} \cdot \mathbf{p}_j), \quad (1)$$

where  $\hat{f}(\mathbf{k})$  represents the Fourier coefficients, encoding the contributions of wave vectors  $\mathbf{k}$  at atom  $j$ . The corresponding inverse transform, which computes  $\hat{f}(\mathbf{k})$  from the real-space representation  $f(\mathbf{p}_j)$ , is given by:

$$\hat{f}(\mathbf{k}) = \frac{1}{\Omega} \sum_{j \in S} h_j \exp(-i\mathbf{k} \cdot \mathbf{p}_j), \quad (2)$$

where  $S$  denotes the set of atomic positions in the crystal lattice,  $h_j$  represents function values at site  $\mathbf{p}_j$  such as nuclear embedding, and  $\Omega$  is the system volume.

### 3 Method

This work focuses on predicting the thermodynamic, electronic, and mechanical properties of crystalline materials through a novel approach that explicitly incorporates long-range interactions from reciprocal space. The architectures of ReGNet and its multi-task variant, ReGNet-MT, are illustrated in Figure 2. Unlike Lin et al. (2023), which employs fixed physical potentials as physics-informed edge features, our approach employs continuous filters with Fourier transforms, utilizing learnable parameters to encode reciprocal space representations while preserving the periodic symmetry of crystalline systems. Inspired by the molecular graph framework in Kosmala et al. (2023), we propose the *ReciprocalBlock*, a specialized module designed to capture long-range interactions in crystalline materials. This module leverages reciprocal lattice vectors and atomic fractional coordinates, eliminating reliance on predefined supercell grid sizes. Therefore, our approach enhances symmetry and periodicity preservation in long-range representations. Besides, we incorporate GNN with our *ReciprocalBlock* to model short- and long-range information in materials. Lastly, we enable a variant multi-property prediction by leveraging mixture-of-experts (MoE) in the decoder.

#### 3.1 Representation and Embedding

**Invariant crystal graph and embedding.** Firstly, we construct a radius-based graph, where nodes represent atoms and edges encode atomic interactions within a predefined cutoff radius  $r_{\text{cut}}$ . Formally, the edge set is defined as:

$$\mathcal{E} = \{e_{ij} : \|\mathbf{p}_i - \mathbf{p}_j\|_2 \leq r_{\text{cut}}, \forall i, j \in V\},$$

where  $V$  is the set of nodes, and distances between nodes are computed based on their 3D Cartesian coordinates  $\mathbf{p}_i$  and  $\mathbf{p}_j$ .

Once the crystal graph is established, we can proceed to obtain embeddings for nodes and edges. Node feature  $\mathbf{a}_i$  for node  $i$  is first mapped using CGCNN (Xie & Grossman, 2018) embeddings, followed by a linear transformation to initialize the short-range node features  $h_{i,\text{local}}^0$ . The initial global atom representation is derived through a linear transformation of  $h_{\text{local}}^0$ , as shown below:

$$h_{\text{global}}^0 = \sigma(W_r h_{\text{local}}^0),$$

where  $W_r$  is a learnable weight matrix. We use  $h_{\text{global}}^0$  as initial long-range node features. The invariant edge feature  $\|\mathbf{p}_i - \mathbf{p}_j\|_2$  is defined by the Euclidean distance between node pair  $i$  and  $j$ , are scaled by  $c/\|\mathbf{p}_i - \mathbf{p}_j\|_2$ , where  $c$  is a chosen constant to mimic the pairwise potential in Lin et al. (2023). These values are then embedded using radial basis function (RBF) kernels to get the initial edge features  $v_{ij}^e$ . More details are shown in Appendix B.2

**Fractional coordinates and reciprocal lattice vectors.** To effectively extract features from long-range information in reciprocal space, we propose using fractional coordinates  $\mathbf{f}$  and basis reciprocal lattice vectors  $\mathbf{k}_m$  with continuous filters convolution. Together, they enable a precise and symmetry-consistent representation of periodic structures (discussed in Section 2). Our approach differs from previous methods (Kosmala et al., 2023) for the following reasons. First, for crystalline materials, Cartesian coordinates can introduce ambiguities, as identical crystal structures may be expressed differently due to periodic transformations, such as translations or rotations. For example, the lattice matrices  $\mathbf{L} = [\ell_1, \ell_2, \ell_3]^\top$  and  $\mathbf{L}' = [\ell_1 + \ell_2, \ell_2, \ell_3]^\top$  describe identical periodic patterns but differ in their Cartesian representations. In contrast, fractional coordinates normalize atomic positions relative to the unit cell, ensuring invariance under periodic transformations and eliminating redundancies in Cartesian representations. Second, it relies on a predefined grid size as hyperparameters to cover all relevant frequencies as  $\mathbf{k}$ , which could disrupt the unit cell symmetry and substantially increase computational costs, particularly for large unit cells and complex systems. Instead, our method leverages the natural periodicity of the lattice in materials, avoiding redundant grid parameterization and ensuring a symmetry-consistent representation of long-range interactions. Therefore, by combining fractional coordinates  $\mathbf{f}$  and basis reciprocal lattice vectors  $\mathbf{k}_m$ , we achieve an effective framework for feature extraction in reciprocal space, accurately capturing the long-range information of crystal materials.

With the aforementioned representations, our model enables both short-range and long-range message passing to effectively capture comprehensive material structural features.

### 3.2 Short-Range Message Passing

We employ the short-range block in Figure 2(b) to update the atomic representations using an invariant graph neural network with multiple message-passing layers. Each node aggregates information only from its geometric neighbors within the cutoff radius  $r_{\text{cut}}$ . Therefore, we naturally interpret this as capturing the short-range information in material representations. The computational process at the  $\ell$ -th message-passing layer for a node  $i$  is expressed as:

$$h_{i,\text{local}}^{\ell+1} \leftarrow g \left( h_{i,\text{local}}^\ell, \sum_{j \in V} \phi(h_{i,\text{local}}^\ell, h_{j,\text{local}}^\ell, v_{ij}^e) \right), \quad (3)$$

where  $h_{i,\text{local}}^\ell$  represents the embedding features of node  $i$  at the  $\ell$ -th layer. Here,  $g$  and  $\phi$  are trainable layers within the GNN. Specifically,  $\phi$  computes interactions between node embeddings and edge features  $v_{ij}^e$ , while  $g$  aggregates these messages to update the node embeddings. Further details on the architecture of the local geometric GNN are provided in Appendix B.

### 3.3 Long-Range Message Passing

To complement the short-range modeling, we employ the long-range block in Figure 2(b) to globally update the atomic representations using the *ReciprocalBlock*. Specifically, this block leverages Fourier transform-based continuous filters with neural networks to encode periodic structures from reciprocal space. Besides, as discussed in Section 3.1, we utilize atomic fractional coordinates  $\mathbf{f}$  and basis reciprocal lattice vectors  $\mathbf{k}_m$  to extract structural information from reciprocal space and update the node features in the model block. The global embeddings are computed iteratively:

$$h_{\text{global}}^{\ell+1} = \text{ReciprocalBlock}(h_{\text{global}}^\ell, \mathbf{f}, \mathbf{k}_m),$$

where  $h_{\text{global}}^\ell$  represents the input embeddings from the  $\ell$ -th layer.

**Reciprocal block.** Here, we explain the reciprocal block in detail. The reciprocal block incorporates long-range interactions into the node embeddings using continuous filters on features derived from Fourier transforms. Each material  $m$  has reciprocal lattice vectors  $\mathbf{k}_m$  based on the lattice vector in real space. The set of atoms in the material is denoted as  $\mathcal{I}_m$ , where  $j \in \mathcal{I}_m$  represents all atoms within material  $m$ . This block aggregates the contributions of all

atoms in each material to compute a global representation in the reciprocal domain. The reciprocal embedding  $r_m$  is computed as:

$$r_m = \sum_{j \in \mathcal{I}_m} h_{j,\text{global}}^\ell \cdot \exp(-i\mathbf{k}_m^\top \mathbf{f}_j),$$

where  $h_{j,\text{global}}^\ell$  is the global embedding of atom  $j$  from  $\ell$ -th layer,  $\mathbf{f}_j$  is its fractional coordinate, and  $i$  is the imaginary unit. This operation aggregates atomic embeddings into a single reciprocal representation for materials, capturing global periodic interactions.

Subsequently, the reciprocal embedding  $r_m$  undergoes an inverse Fourier transform to be mapped back into real space for the atoms in material  $m$ . This process can be expressed as below:

$$\tilde{h}_{\text{global}}^\ell = \sum_{j \in \mathcal{I}_m} \exp(i\mathbf{k}_m^\top \mathbf{f}_j) \cdot r_m \cdot \mathbf{W}_{\text{filter}},$$

where  $\exp(i\mathbf{k}_m^\top \mathbf{f}_j)$  performs the inverse Fourier transform to map the reciprocal representation back to the real domain.  $\mathbf{W}_{\text{filter}}$  is a *trainable filter* refining the reciprocal embedding, selectively emphasizing important contributions from the reciprocal space features to model long-range interactions. In addition, the prefactor  $\frac{1}{\Omega}$  in eq. (2) is incorporated into the learned filter  $\mathbf{W}_{\text{filter}}$ , without requiring explicit normalization by the system volume. In a word, this operation effectively incorporates long-range interactions and periodicity from the reciprocal domain into the real-space representation of each atom  $j \in \mathcal{I}_m$ .

Finally, the global embeddings  $\tilde{h}_{\text{global}}^\ell$  are updated using residual connections to get  $h_{\text{global}}^{\ell+1}$ .

$$h_{\text{global}}^{\ell+1} = h_{\text{global}}^\ell + \tilde{h}_{\text{global}}^\ell.$$

At this point, the complete process of a Reciprocal Block has been fully described.

### 3.4 Hierarchical Embedding Integration

Our model employs multiple ReGNet blocks as message passing layers to integrate local and global information at each layer. Within each block, node embeddings are updated by combining contributions from short-range graph message passing and long-range reciprocal-based message passing. The resulting integrated embeddings, formed by adding up both embedding updates during each message-passing step, are propagated to the next block. This enables the model to iteratively refine hierarchical representations of material structures. This design facilitates the effective capture of both local atomic-scale features and global lattice-scale features throughout the network.

### 3.5 Decoder Block

After completing the iterative message-passing steps, node features are aggregated within each graph using mean pooling, which captures the overall structural information of the material. The resulting graph-level representation is then processed through fully connected layers to predict the target material property. While our novel reciprocal space representations effectively captures long-range interactions and global periodicity, it still predicts properties individually Schütt et al. (2017); Choudhary & DeCost (2021); Yan et al. (2024). Therefore, for higher efficiency, we employ an MTL decoder for multi-property prediction, consisting of MoE layers and task-specific heads. More details can be found in Appendix C.

## 4 Related Work

**Crystal property prediction.** Crystal property prediction has been widely studied using both physics-based and deep-learning approaches. Traditional physics-based methods, such as Coulomb matrices (Rupp et al., 2012; Elton et al., 2018), effectively model ionic and metallic materials but lack generalization due to constraints like permutation

Table 1: Comparison of test MAE on The Materials Project dataset. The best results are highlighted in **bold**, while the second-best results are indicated with underlines.

Method	Formation Energy	Band Gap	Bulk Moduli	Shear Moduli
	meV/atom	eV	log(GPa)	log(GPa)
CGCNN	31	0.292	0.047	0.077
SchNet	33	0.345	0.066	0.099
MEGNET	30	0.307	0.060	0.099
GATGNN	33	0.280	0.045	0.075
ALIGNN	22	0.218	0.051	0.078
Matformer	21.0	0.211	0.043	0.073
PotNet	18.8	0.204	0.040	0.0650
Crystalformer	18.6	0.198	<u>0.0377</u>	0.0689
eComFormer	<u>18.16</u>	0.202	0.0417	0.0729
iComFormer	18.26	<u>0.193</u>	0.0380	<u>0.0637</u>
ReGNet	<b>17.07</b>	<b>0.189</b>	<b>0.0328</b>	<b>0.0628</b>

invariance. Deep learning has introduced more flexible predictions by representing crystals as chemical formulas and using sequence models (Jha et al., 2018; Goodall & Lee, 2020; Wang et al., 2021). More recent methods leverage 3D geometric structures, modeling crystals as 3D graphs with graph neural networks (GNNs) (Schütt et al., 2017; Gastegger et al., 2020). Key advances include CGCNN (Xie & Grossman, 2018), which utilized multi-edge graphs to model periodic invariance, inspiring methods such as ALIGNN (Choudhary & DeCost, 2021), which incorporated angle-based features, and Matformer (Yan et al., 2022), which captured periodic patterns using self-connecting edges. PotNet (Lin et al., 2023) proposed physics-informed edge features that embed the infinite summation of pre-defined interatomic potentials, while Crystalformer (Taniai et al., 2024) encoded periodic structures with infinitely connected attention. Yan et al. (2024) introduced iComFormer with invariant descriptors and eComFormer with equivariant vectors. Despite significant advancements, many approaches still face limitations in accurately capturing periodic patterns and long-range interactions.

**Long-range interaction modeling.** Modeling long-range interactions remains a significant challenge. Early approaches augmented physical equations with hand-crafted terms (Staacke et al., 2021) or predicted atomic charges (Unke et al., 2021), while recent methods focus on data-driven learning. Yu et al. (2022) computed scalar-valued structure factors and integrates them with GNN outputs only in the final layer, limiting interaction between reciprocal space and local features. In contrast, Kosmala et al. (2023) integrated structure factor embeddings directly into GNN message passing, enabling feedback to node embeddings. However, it requires extensive hyperparameter tuning for grid sizes ( $N_x, N_y, N_z$ ) to define the supercell, which can disrupt the symmetry of the unit cell, alter its space group, and substantially increase computational costs, particularly for systems with complex symmetries. Lin et al. (2023) considered the infinite summations of pairwise atomic interactions with additional computational cost  $\mathcal{O}(n^2)$ , relied on precomputed, non-trainable physical potentials as edge features, which limited adaptability to diverse material systems and further increased computational overhead.

**Reciprocal space.** While (Kosmala et al., 2023) incorporates reciprocal space modeling, their approach is tailored to molecular systems and evaluated on semi-periodic surface structures from the OC20 dataset, which includes relaxed small-molecule adsorbates (e.g., CO, H<sub>2</sub>O, NH<sub>3</sub>) on metal surfaces (e.g., Pt, Cu, Ni). These systems lack full 3D periodicity and space group symmetries typical of bulk crystals. As a result, the study does not assess reciprocal space modeling in fully periodic crystalline materials such as perovskites (e.g., SrTiO<sub>3</sub>) or semiconductors (e.g., GaAs), which are typical and important materials. In contrast, our method is explicitly designed for bulk crystals and directly

encodes their symmetry and periodicity. Separately, Taniai et al. (2024) introduces reciprocal space via fixed analytical Fourier-Gaussian formulations within a Transformer-style architecture. However, their reciprocal-space component is non-trainable and presented only as an optional variant in the appendix. Our proposed ReGNet instead employs fully learnable reciprocal-space filters, trained end-to-end to capture long-range interactions beyond the capacity of fixed-function decays.

## 5 Experimental Studies

We evaluate ReGNet on three widely recognized datasets in materials science, Materials Project (Chen et al., 2019), JARVIS-DFT (Choudhary et al., 2020), and MatBench (Dunn et al., 2020). Through extensive experiments, ReGNet demonstrates strong performance across a wide range of crystal properties, highlighting its effectiveness in modeling crystalline materials with reciprocal space.

For JARVIS and MP, to ensure consistency, we adopt experimental settings aligned with prior works, including Matformer (Yan et al., 2022) and PotNet (Lin et al., 2023). These datasets cover a range of scales, including 69239 crystals for large-scale tasks, 18171 crystals for medium-scale tasks, and 5450 crystals for small-scale tasks. To further assess performance, we evaluate ReGNet on the MatBench tasks `e_form` (132752 crystals) and `jdft2d` (636 crystals), following the experimental setup in (Yan et al., 2024). We benchmark against several baseline methods, including CGCNN (Xie & Grossman, 2018), SchNet (Schütt et al., 2017), MEGNet (Chen et al., 2019), GATGNN (Louis et al., 2020), ALIGNN (Choudhary & DeCost, 2021), Matformer (Yan et al., 2022), PotNet (Lin et al., 2023), Crystalformer (Taniai et al., 2024), ComFormer (Yan et al., 2024), MODNet (De Breuck et al., 2021), coGN (Ruff et al., 2024), and M3GNet (Chen & Ong, 2022). All experiments are conducted on NVIDIA A100 GPUs. Additional details on the experimental configurations and implementation settings are provided in Appendix B.

### 5.1 Experimental Results

**The Materials Project (MP)** On the Materials Project dataset, ReGNet consistently outperforms prior methods across all four benchmark tasks, achieving state-of-the-art results with notable improvements. As shown in table 1, ReGNet achieves lower MAE than iComFormer on all target properties, including a 6.5% reduction in formation energy error, 2.1% in bandgap, 13.7% in bulk modulus, and 1.4% in shear modulus.

**JARVIS-DFT** As shown in Table 2, ReGNet surpasses baseline models in formation energy,  $E_{\text{total}}$ , and band gap (MBJ), while achieving competitive results on  $E_{\text{hull}}$  and band gap (OPT). Notably, ReGNet consistently surpasses PotNet across all tasks and improves upon iComFormer with a 7.7% lower MAE on band gap (MBJ) and a 6.9% reduction on total energy prediction.

**MatBench** Experimental results on the MatBench benchmark are summarized in Table 3, reported in terms of MAE and RMSE with standard deviations over five runs. ReGNet achieves state-of-the-art performance on both the large-scale `e_form` task (over 130K crystals) and the small-scale `jdft2d` task (636 crystals), demonstrating strong generalization across both large and limited training data. Notably, it outperforms models that incorporate geometric features such as bond angles, including ALIGNN and M3GNet, as well as coGN, which employs a connectivity-optimized nested graph representation. ReGNet also surpasses MODNet, a leading model based on physical descriptors with feature selection. These results highlight the effectiveness of incorporating reciprocal space information into crystal representations.

*Overall, ReGNet delivers state-of-the-art performance across various crystal property prediction tasks on three widely used crystal benchmarks.* The superior performance of ReGNet can be attributed to several key factors. Notably, ReGNet leverages trainable Fourier filters from reciprocal space to capture long-range interactions while preserving the periodic symmetry of crystal structures, which are fundamental to the accurate and physically grounded representation of crystalline materials. In contrast, prior methods rely on fixed physical forms or predefined grid sizes that require



Table 2: Comparison of test MAE on the JARVIS dataset. The best results are highlighted in **bold**, and the second-best results are indicated with underlines. Lower test MAE indicates better results.

Method	Form. Energy	Bandgap(OPT)	$E_{total}$	Bandgap(MBJ)	$E_{hull}$
	meV/atom	eV	meV/atom	eV	meV
CGCNN	63	0.20	78	0.41	170
SchNet	45	0.19	47	0.43	140
MEGNET	47	0.145	58	0.34	84
GATGNN	47	0.170	56	0.51	120
ALIGNN	33.1	0.142	37	0.31	76
Matformer	32.5	0.137	35	0.30	64
PotNet	29.4	0.127	32	0.27	55
Crystalformer	30.6	0.128	32	0.27	46
eComFormer	28.4	<u>0.124</u>	32	0.28	<u>44</u>
iComFormer	<u>27.2</u>	<b>0.122</b>	<u>28.8</u>	<u>0.26</u>	47
ReGNet	<b>27.0</b>	0.126	<b>26.8</b>	<b>0.24</b>	<b>43</b>

Table 3: Comparison on MatBench. The best results are highlighted in **bold**, and the second-best results are indicated with underlines. Lower test MAE and test RMSE indicate better results.

Method	e_form-132752 (meV/atom)		jdf2d-636 (meV/atom)	
	MAE	RMSE	MAE	RMSE
MODNet	44.8 $\pm$ 3.9	88.8 $\pm$ 7.5	<u>33.2 <math>\pm</math> 7.3</u>	96.7 $\pm$ 40.4
ALIGNN	21.5 $\pm$ 0.5	55.4 $\pm$ 5.5	43.4 $\pm$ 8.9	117.4 $\pm$ 42.9
coGN	17.0 $\pm$ 0.3	48.3 $\pm$ 5.9	37.2 $\pm$ 13.7	101.2 $\pm$ 55.0
M3GNet	19.5 $\pm$ 0.2	-	50.1 $\pm$ 11.9	-
eComFormer	<u>16.5 <math>\pm</math> 0.3</u>	45.4 $\pm$ 4.7	37.8 $\pm$ 9.0	102.2 $\pm$ 46.4
iComFormer	<u>16.5 <math>\pm</math> 0.3</u>	<u>43.2 <math>\pm</math> 3.7</u>	34.8 $\pm$ 9.9	<u>96.1 <math>\pm</math> 46.3</u>
ReGNet	<b>16.1 <math>\pm</math> 0.2</b>	<b>42.9 <math>\pm</math> 3.5</b>	<b>31.6 <math>\pm</math> 6.3</b>	<b>75.6 <math>\pm</math> 34.7</b>

tuning. Besides, by integrating reciprocal-space-based global information with GNN-driven local modeling, ReGNet provides a comprehensive representation of crystalline materials.

## 5.2 Ablation Studies

Table 4: Ablation studies of reciprocal space and model depth in test MAE on the JARVIS dataset.

Method	Reciprocal	Blocks	Form. Energy	Bandgap(OPT)	$E_{total}$	Bandgap(MBJ)	$E_{hull}$
ReGNet w/o Reciprocal	<b>✗</b>	3	29.6	0.135	32.5	0.295	68.8
ReGNet	<b>✓</b>	3	27.8	0.127	27.2	0.242	52.9
ReGNet	<b>✓</b>	4	<b>27.0</b>	<b>0.126</b>	<b>26.8</b>	<b>0.239</b>	<b>48.0</b>

In this section, we examine the importance of incorporating reciprocal space and analyze the effect of the number of ReGNet blocks through ablation studies on the JARVIS dataset. Specifically, we evaluate a variant of ReGNet with the reciprocal space component removed. As shown in Table 4, including reciprocal space information leads to improved

performance. Furthermore, increasing the number of ReGNet blocks from 3 to 4 yields additional gains on the JARVIS benchmark. Additional ablation results are provided in Appendix B.5.

### 5.3 Multi-property prediction

ReGNet-MT achieves promising performance with much higher efficiency. On the Materials Project dataset, we apply two ReGNet-MT models separately for predicting two energy properties and two mechanical properties. It achieves comparable performance as shown in Table 13 in the Appendix. For the JARVIS dataset, ReGNet-MT on 5-property prediction delivers the best results for band gap (OPT) and band gap (MBJ), outperforming all single-property prediction models, while maintaining comparable performance on the remaining tasks to Matformer as shown in Table 12, which benefits from positive transfer as discussed in Appendix C.5. Besides, its efficiency is discussed in Section 5.4.

### 5.4 Model Efficiency Comparison

This section highlights the efficiency of ReGNet in handling both single-task and multi-task scenarios. As shown in Table 5, we evaluate the computational efficiency of ReGNet and ReGNet-MT by comparing their model parameters and training time per epoch against ALIGNN, Matformer, PotNet, and ComFormer on the JARVIS formation energy task. We use 3 and 4 to indicate the number of blocks in ReGNet. ReGNet demonstrates superior computational efficiency, with ReGNet(3) achieving the fastest training time per epoch among all models. Notably, in the multi-task setting, ReGNet-MT predicts five properties simultaneously. The training time does not even double that of single-task ReGNet, and the model’s parameter size is smaller than that of single-task eComFormer. It is also important to note that PotNet reduces its training time by precomputing infinite potential summations for the training data, which is not employed in ReGNet.

Table 5: Comparison of model efficiency on JARVIS formation energy prediction. We include training time per epoch, 1-task model parameter size, and 5-task model parameter size. N/A denotes that ReGNet-MT is not designed for single-property prediction.

Method	Type	Time/Epoch	1-task Model Para.	5-task Model Para.
ALIGNN	GNN	261 s	4.0 M	20.0 M
Matformer	Transformer	51 s	2.9 M	14.5 M
PotNet	GNN	34 s	1.8 M	9.0 M
iComFormer	Transformer	62 s	5.0 M	25.0 M
eComFormer	Transformer	92 s	12.4 M	62.0 M
ReGNet(3)	GNN	31 s	3.3 M	16.5 M
ReGNet(4)	GNN	38 s	4.3 M	21.5 M
ReGNet-MT	GNN	60 s	N/A	9.5 M

## 6 Limitation

One limitation of our study lies in using geometric GNNs for short-range modeling to capture local features. While effective, recent advancements in Transformer-based models (Yan et al., 2022, 2024) present opportunities for further improvement by incorporating reciprocal space information to enhance the structural representation of materials. Besides, multi-property prediction remains an area worthy of further exploration, as current extensions only provide an initial attempt. Despite these limitations, our study provides a new perspective on modeling crystal materials by leveraging long-range information from reciprocal space alongside graph-based short-range information.

## 7 Conclusion

In this paper, we introduce a novel model, ReGNet, designed to capture the reciprocal space-based long-range information and geometric short-range information in crystal property prediction. Besides, its multi-task variant with the help of MoE has achieved promising results in multi-property prediction. Empirically, ReGNet achieves significant performance improvement on three widely used crystal benchmarks. We hope this efficient model provides a valuable perspective to both machine learning and materials science, promoting further interdisciplinary research and encouraging its application across diverse material systems as a foundational component.

## References

- Neil W. Ashcroft and N. David Mermin. *Solid State Physics*. Harcourt College Publishers, 2001.
- Neil W Ashcroft, N David Mermin, and Sergio Rodriguez. Solid state physics. *American Journal of Physics*, 46(1): 116–117, 1978.
- Dominique Beaini, Shenyang Huang, Joao Alex Cunha, Zhiyi Li, Gabriela Moisesescu-Pareja, Oleksandr Dymov, Samuel Maddrell-Mander, Callum McLean, Frederik Wenkel, Luis Müller, et al. Towards foundational models for molecular learning on large-scale multi-task datasets. *arXiv preprint arXiv:2310.04292*, 2023.
- Chi Chen and Shyue Ping Ong. A universal graph deep learning interatomic potential for the periodic table. *Nature Computational Science*, 2(11):718–728, 2022.
- Chi Chen, Weike Ye, Yunxing Zuo, Chen Zheng, and Shyue Ping Ong. Graph networks as a universal machine learning framework for molecules and crystals. *Chemistry of Materials*, 31(9):3564–3572, 2019.
- Kamal Choudhary and Brian DeCost. Atomistic line graph neural network for improved materials property predictions. *npj Computational Materials*, 7(1):185, 2021.
- Kamal Choudhary, Kevin F Garrity, Andrew CE Reid, Brian DeCost, Adam J Biacchi, Angela R Hight Walker, Zachary Trautt, Jason Hattrick-Simpers, A Gilad Kusne, Andrea Centrone, et al. The joint automated repository for various integrated simulations (jarvis) for data-driven materials design. *npj computational materials*, 6(1):173, 2020.
- Kamal Choudhary, Brian DeCost, Chi Chen, Anubhav Jain, Francesca Tavazza, Ryan Cohn, Cheol Woo Park, Alok Choudhary, Ankit Agrawal, Simon JL Billinge, et al. Recent advances and applications of deep learning methods in materials science. *npj Computational Materials*, 8(1):59, 2022.
- Dimitrios Christofidellis, Giorgio Giannone, Jannis Born, Ole Winther, Teodoro Laino, and Matteo Manica. Unifying molecular and textual representations via multi-task language modelling. In *International Conference on Machine Learning*, pp. 6140–6157. PMLR, 2023.
- Bernard Dennis Cullity and R Smoluchowski. Elements of x-ray diffraction. *Physics Today*, 10(3):50–50, 1957.
- Pierre-Paul De Breuck, Geoffroy Hautier, and Gian-Marco Rignanese. Materials property prediction for limited datasets enabled by feature selection and joint learning with modnet. *npj computational materials*, 7(1):83, 2021.
- Alexander Dunn, Qi Wang, Alex Ganose, Daniel Dopp, and Anubhav Jain. Benchmarking materials property prediction methods: the matbench test set and automatminer reference algorithm. *npj Computational Materials*, 6(1):138, 2020.
- Eleftherios N. Economou. *The Physics of Solids*. Springer, 2010.
- Ray F Egerton et al. *Physical principles of electron microscopy*, volume 56. Springer, 2005.

- Daniel C Elton, Zois Boukouvalas, Mark S Butrico, Mark D Fuge, and Peter W Chung. Applying machine learning techniques to predict the properties of energetic materials. *Scientific reports*, 8(1):9059, 2018.
- Theodoros Evgeniou and Massimiliano Pontil. Regularized multi-task learning. In *Proceedings of the tenth ACM SIGKDD international conference on Knowledge discovery and data mining*, pp. 109–117, 2004.
- Johannes Gasteiger, Janek Groß, and Stephan Günnemann. Directional message passing for molecular graphs. *arXiv preprint arXiv:2003.03123*, 2020.
- Rhys EA Goodall and Alpha A Lee. Predicting materials properties without crystal structure: deep representation learning from stoichiometry. *Nature communications*, 11(1):6280, 2020.
- Richard Gross and Achim Marx. *Festkörperphysik*. De Gruyter, 2014.
- RW James. The dynamical theory of x-ray diffraction. In *Solid State Physics*, volume 15, pp. 53–220. Elsevier, 1963.
- Dipendra Jha, Logan Ward, Arindam Paul, Wei-keng Liao, Alok Choudhary, Chris Wolverton, and Ankit Agrawal. Elemnet: Deep learning the chemistry of materials from only elemental composition. *Scientific reports*, 8(1):17593, 2018.
- Robert O Jones. Density functional theory: Its origins, rise to prominence, and future. *Reviews of modern physics*, 87(3):897–923, 2015.
- Diederik P Kingma. Adam: A method for stochastic optimization. *arXiv preprint arXiv:1412.6980*, 2014.
- Arthur Kosmala, Johannes Gasteiger, Nicholas Gao, and Stephan Günnemann. Ewald-based long-range message passing for molecular graphs. In *International Conference on Machine Learning*, pp. 17544–17563. PMLR, 2023.
- Marcus Frederick Charles Ladd, Rex Alfred Palmer, and Rex Alfred Palmer. *Structure determination by X-ray crystallography*, volume 233. Springer, 1977.
- Yuchao Lin, Keqiang Yan, Youzhi Luo, Yi Liu, Xiaoning Qian, and Shuiwang Ji. Efficient approximations of complete interatomic potentials for crystal property prediction. In *International Conference on Machine Learning*, pp. 21260–21287. PMLR, 2023.
- Shengchao Liu, Meng Qu, Zuobai Zhang, Huiyu Cai, and Jian Tang. Structured multi-task learning for molecular property prediction. In *International conference on artificial intelligence and statistics*, pp. 8906–8920. PMLR, 2022.
- Steph-Yves Louis, Yong Zhao, Alireza Nasiri, Xiran Wang, Yuqi Song, Fei Liu, and Jianjun Hu. Graph convolutional neural networks with global attention for improved materials property prediction. *Physical Chemistry Chemical Physics*, 22(32):18141–18148, 2020.
- Kenneth R Poeppelmeier. *Comprehensive Inorganic Chemistry III*. Elsevier, 2023.
- Yuxuan Ren, Dihan Zheng, Chang Liu, Peiran Jin, Yu Shi, Lin Huang, Jiyan He, Shengjie Luo, Tao Qin, and Tie-Yan Liu. Physical consistency bridges heterogeneous data in molecular multi-task learning. *arXiv preprint arXiv:2410.10118*, 2024.
- Carlos Riquelme, Joan Puigcerver, Basil Mustafa, Maxim Neumann, Rodolphe Jenatton, André Susano Pinto, Daniel Keysers, and Neil Houlsby. Scaling vision with sparse mixture of experts. *Advances in Neural Information Processing Systems*, 34:8583–8595, 2021.
- Robin Ruff, Patrick Reiser, Jan Stühmer, and Pascal Friederich. Connectivity optimized nested line graph networks for crystal structures. *Digital Discovery*, 3(3):594–601, 2024.

- Matthias Rupp, Alexandre Tkatchenko, Klaus-Robert Müller, and O Anatole Von Lilienfeld. Fast and accurate modeling of molecular atomization energies with machine learning. *Physical review letters*, 108(5):058301, 2012.
- Kristof Schütt, Pieter-Jan Kindermans, Huziel Enoc Saucedo Felix, Stefan Chmiela, Alexandre Tkatchenko, and Klaus-Robert Müller. Schnet: A continuous-filter convolutional neural network for modeling quantum interactions. *Advances in neural information processing systems*, 30, 2017.
- Kristof T Schütt, Huziel E Saucedo, P-J Kindermans, Alexandre Tkatchenko, and K-R Müller. Schnet—a deep learning architecture for molecules and materials. *The Journal of Chemical Physics*, 148(24), 2018.
- Noam Shazeer, Azalia Mirhoseini, Krzysztof Maziarz, Andy Davis, Quoc Le, Geoffrey Hinton, and Jeff Dean. Outrageously large neural networks: The sparsely-gated mixture-of-experts layer. *arXiv preprint arXiv:1701.06538*, 2017.
- Leslie N Smith and Nicholay Topin. Super-convergence: Very fast training of neural networks using large learning rates. In *Artificial intelligence and machine learning for multi-domain operations applications*, volume 11006, pp. 369–386. SPIE, 2019.
- Carsten G Staacke, Hendrik H Heenen, Christoph Scheurer, Gábor Csányi, Karsten Reuter, and Johannes T Margraf. On the role of long-range electrostatics in machine-learned interatomic potentials for complex battery materials. *ACS Applied Energy Materials*, 4(11):12562–12569, 2021.
- Tatsunori Tanai, Ryo Igarashi, Yuta Suzuki, Naoya Chiba, Kotaro Saito, Yoshitaka Ushiku, and Kanta Ono. Crystal-former: infinitely connected attention for periodic structure encoding. *arXiv preprint arXiv:2403.11686*, 2024.
- Oliver T Unke, Stefan Chmiela, Michael Gastegger, Kristof T Schütt, Huziel E Saucedo, and Klaus-Robert Müller. Spookynet: Learning force fields with electronic degrees of freedom and nonlocal effects. *Nature communications*, 12(1):7273, 2021.
- Anthony Yu-Tung Wang, Steven K Kauwe, Ryan J Murdock, and Taylor D Sparks. Compositionally restricted attention-based network for materials property predictions. *Npj Computational Materials*, 7(1):77, 2021.
- Peiyao Xiao, Hao Ban, and Kaiyi Ji. Direction-oriented multi-objective learning: Simple and provable stochastic algorithms. *Advances in Neural Information Processing Systems*, 36, 2024.
- Tian Xie and Jeffrey C Grossman. Crystal graph convolutional neural networks for an accurate and interpretable prediction of material properties. *Physical review letters*, 120(14):145301, 2018.
- Keqiang Yan, Yi Liu, Yuchao Lin, and Shuiwang Ji. Periodic graph transformers for crystal material property prediction. *Advances in Neural Information Processing Systems*, 35:15066–15080, 2022.
- Keqiang Yan, Cong Fu, Xiaofeng Qian, Xiaoning Qian, and Shuiwang Ji. Complete and efficient graph transformers for crystal material property prediction. *arXiv preprint arXiv:2403.11857*, 2024.
- Hongyu Yu, Liangliang Hong, Shiyu Chen, Xingao Gong, and Hongjun Xiang. Capturing long-range interaction with reciprocal space neural network. *arXiv preprint arXiv:2211.16684*, 2022.
- Claudio Zeni, Robert Pinsler, Daniel Zügner, Andrew Fowler, Matthew Horton, Xiang Fu, Sasha Shysheya, Jonathan Crabbé, Lixin Sun, Jake Smith, et al. Mattergen: a generative model for inorganic materials design. *arXiv preprint arXiv:2312.03687*, 2023.
- John M Ziman. *Electrons and phonons: the theory of transport phenomena in solids*. Oxford university press, 2001.

## A Reciprocal Space Concepts

### A.1 Relations Between Real and Reciprocal Lattice Vectors

In materials science, crystals exhibit translational symmetry, where atoms are periodically arranged in 3D space, forming a direct lattice in real space. Each lattice point corresponds to a repeating unit in the crystal structure, described by primitive lattice vectors  $\ell_1, \ell_2, \ell_3$ . Reciprocal space, on the other hand, represents the spatial frequencies associated with this periodic arrangement. It forms a dual lattice, mathematically related to the real lattice through reciprocal lattice vectors  $\mathbf{b}_1, \mathbf{b}_2, \mathbf{b}_3$ .  $V$  is the volume of the parallelepiped spanned by the three primitive translation vectors of the original Bravais lattice. It remains invariant under periodic permutations of the indices (Economou, 2010).

Volume and vectors are defined as:

$$V = \ell_1 \cdot (\ell_2 \times \ell_3) \quad (4)$$

$$\mathbf{b}_1 = 2\pi \cdot \frac{\ell_2 \times \ell_3}{V} \quad (5)$$

$$\mathbf{b}_2 = 2\pi \cdot \frac{\ell_3 \times \ell_1}{V} \quad (6)$$

$$\mathbf{b}_3 = 2\pi \cdot \frac{\ell_1 \times \ell_2}{V} \quad (7)$$

These vectors satisfy the reciprocal relationship:

$$\ell_i \cdot \mathbf{b}_j = 2\pi \delta_{ij}. \quad (8)$$

The symbol  $\delta_{ij}$  represents the Kronecker delta, which is a mathematical function defined as:

$$\delta_{ij} = \begin{cases} 1, & \text{if } i = j \\ 0, & \text{if } i \neq j \end{cases} \quad (9)$$

This allows us to define a periodic function naturally in reciprocal space, where vectors  $\mathbf{k} \in \Lambda$  can be expanded in terms of these reciprocal basis vectors (Ashcroft & Mermin, 2001).

The 3D spatial frequencies must be integer combinations of *three* spatial basis frequencies  $\mathbf{b}_1, \mathbf{b}_2, \mathbf{b}_3 \in \mathbb{R}^{3 \times 3}$  spanning the *reciprocal lattice*:

$$\Lambda = \{n'_1 \mathbf{b}_1 + n'_2 \mathbf{b}_2 + n'_3 \mathbf{b}_3 | n'_1, n'_2, n'_3 \in \mathbb{Z}\}. \quad (10)$$

### A.2 Diffraction Methods

Reciprocal space is fundamental to diffraction techniques such as X-ray diffraction (XRD) and electron diffraction. XRD is a widely used technique in crystallography that examines the constructive interference of X-rays scattered by periodic atomic planes, providing detailed insights into crystal structures (Ladd et al., 1977). Similarly, in electron diffraction, the elastic scattering of electrons by atoms produces diffraction patterns that reveal structural information (Egerton et al., 2005). The scattering intensity is modeled using the structure factor:

$$S(\mathbf{G}) = \sum_j f_j e^{-i\mathbf{G} \cdot \mathbf{r}_j} \quad (11)$$

where  $\mathbf{G}$  is the reciprocal lattice vector.  $f_j$  represents the atomic form factor in X-ray diffraction, and the electron scattering factor in electron diffraction separately. Diffraction patterns are governed by Bragg's law:

$$n\lambda = 2d \sin \theta, \quad (12)$$

relating lattice spacings ( $d$ ) to diffraction angles ( $\theta$ ) and wavelength ( $\lambda$ ) (Cullity & Smoluchowski, 1957). Notably, this condition applies to both XRD and ED, although electron diffraction often requires consideration of dynamical scattering effects due to stronger interactions between electrons and matter (James, 1963).

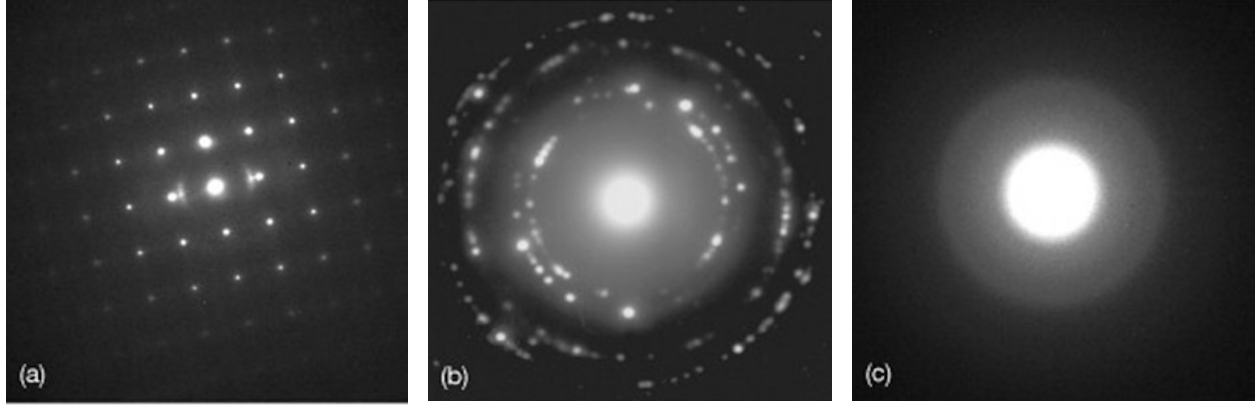


Figure 3: Example of electron diffraction patterns from Poeppelmeier (2023).

Electron diffraction is widely used in transmission electron microscopy (TEM) to analyze materials. For instance, single crystals produce discrete spot patterns, polycrystals form concentric rings, and amorphous materials show diffuse rings (Egerton et al., 2005). These patterns enable crystallinity and orientation analysis, with applications in semiconductors, metals, and oxides. Figure 3 illustrates a typical diffraction pattern. By satisfying the Bragg condition, elastically scattered electrons produce high-intensity spots, with the angular relationship between transmitted and diffracted beams revealing the crystal structure (Poeppelmeier, 2023).

### A.3 Electronic Band

Reciprocal space plays a crucial role in determining electronic and vibrational properties. Specifically, Bloch’s theorem relates the electron wavefunction  $\psi(\mathbf{r})$  to the wave vector  $\mathbf{k}$  as:

$$\psi(\mathbf{r}) = e^{i\mathbf{k}\cdot\mathbf{r}}u(\mathbf{r}) \quad (13)$$

where  $\psi(\mathbf{r})$  is the electronic wavefunction,  $\mathbf{k}$  is the wave vector in reciprocal space. This theorem facilitates the study of electronic band structures, enabling the prediction of properties like band gaps and carrier mobility (Ashcroft et al., 1978).

$u(\mathbf{r})$  is a function periodic with the lattice, and  $\mathbf{r}$  denotes position:

$$u(\mathbf{r} + \mathbf{R}) = u(\mathbf{r}) \quad (14)$$

with  $\mathbf{R}$  being a lattice translation vector. This decomposition separates the plane wave component, representing long-range propagation, and the periodic modulation, capturing local interactions within the unit cell.

The energy eigenvalues, plotted as a function of  $\mathbf{k}$  within the first Brillouin zone (Ashcroft & Mermin, 2001), form a band structure that determines key material properties, including band gaps which distinguish insulators, semiconductors, and metals, effective mass and carrier mobility which influence electronic conductivity, and optical absorption spectra and dielectric constants which govern photon-electron interactions and optoelectronic performance (Ziman, 2001).

## B Experimental Details

### B.1 Dataset

We provide more details for the JARVIS, Materials Project, and MatBench datasets in this section.

Table 6: Dataset sizes vary for different properties.

Dataset	Task	Total
JARVIS-DFT	Formation Energy	55722
	Bandgap (OPT)	55722
	Total Energy	55722
	Bandgap (MBJ)	18171
	$E_{\text{hull}}$	55370
Materials Project	Formation Energy	69239
	Band Gap	69239
	Bulk Moduli	5450
	Shear Moduli	5450
MatBench	e_form	132752
	jdft2d	636

**JARVIS Dataset** The JARVIS dataset, proposed by Choudhary et al. (2020), contains 55723 materials and serves as a benchmark for crystal property prediction. Following the experimental protocols of Yan et al. (2024), we evaluate our methods on five regression tasks: formation energy, total energy, bandgap (using both OPT and MBJ methods), and energy above the convex hull (Ehull). The training, validation, and testing splits for formation energy, total energy, and OPT bandgap consist of 44578, 5572, and 5572 crystals, respectively. The splits for Ehull include 44296, 5537, and 5537 crystals, while the MBJ bandgap tasks consist of 14537, 1817, and 1817 crystals. The MBJ functional is considered more accurate for bandgap calculations compared to OPT, and both are utilized in this study. Notably, 18865 of the dataset’s crystal structures have been experimentally observed, adding robustness to its use in predictive modeling.

**The Materials Project Dataset** The Materials Project dataset, introduced by Chen et al. (2019), is a comprehensive collection of 69239 materials, widely utilized in crystal property prediction studies. We adopt the data splits in Yan et al. (2024) to ensure consistency and fair comparisons with prior methods. Specifically, for formation energy and bandgap prediction tasks, the dataset comprises 60000, 5000, and 4239 crystals for training, validation, and testing, respectively. For bulk modulus and shear modulus predictions, the splits include 4664, 393, and 393 crystals. Notably, one validation sample in the shear modulus task is excluded due to a negative GPa value, reflecting an underlying unstable or metastable crystal structure. Among the included crystals, 30084 have been experimentally observed, further highlighting the dataset’s reliability for studying material properties.

**MatBench Dataset** The Matbench dataset Dunn et al. (2020) is a benchmark suite designed for evaluating machine learning models on materials science tasks, offering standardized splits and diverse property predictions. In this work, we focus on two representative regression tasks from Matbench: the large-scale formation energy prediction task (e\_form) comprising 132752 crystal structures, and the smaller-scale 2D exfoliation energy task (jdft2d) with 636 samples. These tasks assess the model’s ability to generalize across both abundant and limited data regimes.

## B.2 Settings of Model Embeddings

Node feature is embedded into a CGCNN (Xie & Grossman, 2018) embedding vector of length 92 based on atomic number, and then mapped to a 256-dimensional initial short-range node feature  $h_{\text{local}}^0$  by a linear transformation. The initial global node feature  $h_{\text{global}}^0$  is obtained by a linear transformation on  $h_{\text{local}}^0$  and follows an activation function. The invariant edge feature  $\|\mathbf{p}_i - \mathbf{p}_j\|_2$  is inversely scaled to  $-0.75/\|\mathbf{p}_i - \mathbf{p}_j\|_2$  based on Lin et al. (2023), and then



expanded into a 256-dimensional vector by RBF kernels with 256 center values from -4.0 to 4.0; after that, we transfer the 256-dimensional vector to initial edge feature  $v_{ij}^e$  through a linear transformation followed by a SoftPlus activation.

### B.3 Geometric GNN Information

Building on PotNet (Lin et al., 2023), we adopt its base model as the local graph component, without using its additional computed infinite summation of interatomic potentials. The local module performs iterative message passing over the constructed graph using a sequence of graph convolutional layers. Each layer updates node features  $h$  by aggregating information from neighboring nodes and edge attributes. At layer  $l$ , messages are constructed by concatenating features of neighboring nodes and edge attributes:

$$\mathbf{z}_{ij}^{(l)} = [h_i^{(l)} \| h_j^{(l)} \| v_{ij}^e] \in \mathbb{R}^{3d}, \quad (15)$$

where  $h_i^{(l)}$  and  $h_j^{(l)}$  are node embeddings of nodes  $i$  and  $j$ , respectively,  $d_{ij}$  is the edge attribute, and  $\|$  denotes concatenation. These concatenated features are processed by a multi-layer perceptron to compute attention coefficients that regulate the influence of neighboring nodes:

$$\beta_{ij}^{(l)} = \text{Sigmoid} \left( \text{BN} \left( \text{MLP} \left( \mathbf{z}_{ij}^{(l)} \right) \right) \right) \in \mathbb{R}^d, \quad (16)$$

where  $\beta_{ij}^{(l)}$  denotes the local attention coefficient. Messages are then aggregated from neighbors using a weighted sum:

$$\tilde{h}_i^{(l)} = \text{Aggregation} \left( \beta_{ij}^{(l)} \odot \text{MLP} \left( \mathbf{z}_{ij}^{(l)} \right) \right) \in \mathbb{R}^d, \quad (17)$$

with  $\odot$  as the Hadamard product and the aggregation operator performing sum or mean pooling. The updated embeddings are computed via residual connections with batch normalization and activation:

$$h_i^{(l+1)} = \text{ReLU} \left( h_i^{(l)} + \text{BN} \left( \tilde{h}_i^{(l)} \right) \right) \in \mathbb{R}^d. \quad (18)$$

### B.4 Hyperparameter Settings of ReGNet on Different Tasks

In this subsection, we share the detailed hyperparameter settings of ReGNet and ReGNet-MT for different tasks in JARVIS, the Materials Project, and MatBench crystal datasets. We use a different number of blocks for different tasks, and higher performance is expected if hyperparameters are tuned specifically for each task.

Table 7: Model settings of ReGNet for the JARVIS dataset.

	Num. blocks	Total epochs	Learning rate	Num. neighbors
formation energy	4	500	0.0008	16
band gap (OPT)	4	500	0.0006	16
band gap (MBJ)	3	500	0.001	16
total energy	4	500	0.0008	16
Ehull	5	500	0.0006	16

**JARVIS.** We show the model settings of ReGNet on the JARVIS dataset in Table 7. We train both models using the Adam (Kingma, 2014) optimizer with weight decay of  $1e-5$ , OneCycle scheduler (Smith & Topin, 2019), and for a duration of 500 training epochs. The batch size is standardized at 64, and the models are trained using L1 loss function. The effectiveness of the model is quantitatively measured using the mean absolute error (MAE). The number of neighbors indicates the  $k$ -th nearest distance we use as the radius for node  $i$ .

**The Materials Project.** We show the model settings of ReGNet on the Materials Project dataset in Table 8. We train both models using the Adam (Kingma, 2014) optimizer with weight decay of  $1e-5$ , and the OneCycle scheduler

Table 8: Model settings of ReGNet for the Materials Project dataset.

	Num. blocks	Total epochs	Learning rate	Num. neighbors
formation energy	3	500	0.0008	16
band gap	3	500	0.0008	16
bulk moduli	3	500	0.001	16
shear moduli	3	300	0.001	16

Table 9: Model settings of ReGNet-MT for JARVIS and the Materials Project datasets.

	# blocks	Total epochs	Learning rate	# neighbors
JARVIS	3	500	0.0008	16
Materials Project-(form. energy+band gap)	3	500	0.0008	16
Materials Project-(bulk+shear moduli)	3	300	0.001	16

Table 10: Model settings of ReGNet for MatBench.

	Num. blocks	Total epochs	Learning rate	Num. neighbors
e_form	5	500	0.0004	16
jdft2d	3	500	0.001	16

(Smith & Topin, 2019). The batch size is standardized at 64, and the models are trained using L1 loss function. The effectiveness of the model is quantitatively measured using the mean absolute error (MAE). The number of training epochs for shear moduli on ReGNet is 300, while for the other three properties it is 500.

**MatBench.** We show the model settings of ReGNet on the MatBench dataset in Table 10. All models are trained for 500 epochs using the Adam (Kingma, 2014) optimizer with MAE loss. The effectiveness of the models is quantitatively measured using the mean absolute error (MAE) and root mean square error (RMSE).

## B.5 Detailed Ablation Studies

We further investigate the effect of model depth by varying the number of ReGNet blocks from 3 to 5. As shown in Table 11, increasing the number of blocks from 3 to 4 consistently improves performance across all tasks. Performance on  $E_{\text{hull}}$  continues to improve with five blocks, suggesting that deeper message passing may help capture the subtle energy differences relevant to thermodynamic stability. However, for other properties on the JARVIS dataset, adding a fifth block offers no additional benefit and leads to slight performance degradation. This suggests that while increased depth enhances representational capacity, it may also introduce overfitting or optimization difficulties, especially when training data is limited. To balance predictive accuracy and computational cost, we adopt three or four ReGNet blocks as the default configuration.

## B.6 Training Time Scale Efficiency Analysis

Beyond the superior modeling capacity for crystalline materials, our ReGNet is faster and more efficient than previous works. To demonstrate the efficiency of ReGNet, we compare ReGNet and its multi-task variant ReGNet-MT with iComFormer, eComFormer, PotNet, Matformer, and ALIGNN. Evaluation is in terms of training time per epoch on the task of JARVIS formation energy prediction. From Figure 4, ReGNet demonstrates superior computational efficiency. Specifically, ReGNet(3) outperforms iComFormer by  $1.77\times$ , eComFormer by  $2.96\times$ , PotNet by  $1.08\times$ , Matformer by  $1.65\times$ , and ALIGNN by  $8.41\times$  speedup. Finally, the time for ReGNet-MT predicting 5 properties does not even double.

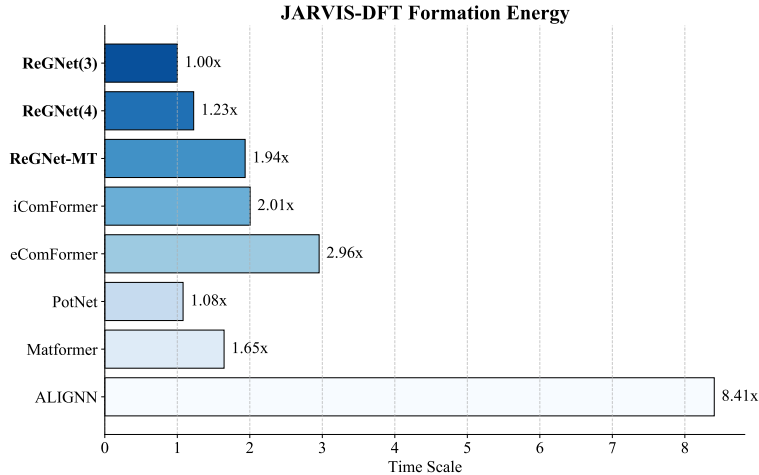


Figure 4: Efficiency comparison of training time per epoch, with each method’s training time scaled relative to ReGNet(3). 3 and 4 indicate the number of ReGNet blocks.

Table 11: Ablation study of ReGNet with varying model depth, reported in terms of test MAE on the JARVIS dataset. The numbers 3, 4, and 5 denote the number of ReGNet blocks used. The best results are shown in **bold**.

Method	Form. Energy	Bandgap(OPT)	$E_{\text{total}}$	Bandgap(MBJ)	$E_{\text{hull}}$
	meV/atom	eV	meV/atom	eV	meV
ReGNet(3)	27.8	0.127	27.2	0.242	52.9
ReGNet(4)	<b>27.0</b>	<b>0.126</b>	<b>26.8</b>	<b>0.239</b>	48.0
ReGNet(5)	27.7	0.127	27.2	0.240	<b>43.0</b>

These results highlight the effectiveness of ReGNet in reducing computational overhead while maintaining performance in prediction, as previously mentioned.

## C Multi-task Learning

### C.1 Motivation

While our novel usage of reciprocal space representations effectively captures long-range interactions and global periodicity, it still adheres to the traditional approach of predicting properties individually Schütt et al. (2017); Choudhary & DeCost (2021); Yan et al. (2024). This approach becomes computationally and memory inefficient when repeatedly applied to multi-property predictions. To address this limitation, Multi-Task Learning (MTL) offers a promising solution by enabling the prediction of multiple properties within a single model Evgeniou & Pontil (2004). Additionally, MTL can leverage positive transfer, where knowledge and representations learned from one task can benefit other tasks. This advantage is particularly relevant for materials, as similar properties (e.g., OPT bandgap and MBJ bandgap) are often highly correlated and share similar structural features. However, to our knowledge, few studies have specifically investigated multi-property prediction for materials.

Table 12: Comparison of MTL on JARVIS in terms of test MAE. N/A denotes that the property is not involved in the prediction.

Method	Form. Energy	Bandgap(OPT)	$E_{\text{total}}$	Bandgap(MBJ)	$E_{\text{hull}}$
	meV/atom	eV	meV/atom	eV	meV
ReGNet-MT	<b>35.0</b>	<b>0.122</b>	<b>36.0</b>	<b>0.21</b>	<b>69.2</b>
ReGNet-LS (3 tasks)	37.0	0.127	37.3	N/A	N/A
ReGNet-LS (5 tasks)	49.9	0.136	53.0	0.24	92.1

## C.2 Related Works on Multi-property prediction

While multi-property prediction in materials remains largely unexplored, we summarize several advances in molecular domains. Liu et al. (2022) introduced the MTL concept in molecular property prediction in the early stage. Their approach involves constructing a sparse dataset and relying on prior knowledge of property relations before training. Christofidellis et al. (2023) proposed a language model that bridges natural and chemical languages to perform multi-task learning, such as chemical reaction prediction and retrosynthesis. However, their work is not specifically focused on multi-property prediction. Additionally, Beaini et al. (2023) developed a foundation model and a large-scale molecular dataset tailored for multi-task learning. Nevertheless, there is currently no comparably large material dataset to support a similar effort. In another approach, Ren et al. (2024) leveraged physical laws after task decoders to address data heterogeneity across different properties, improving prediction consistency. In contrast, we integrate the Mixture of Experts (MoE) between encoders and decoders, allowing each task to obtain customized structural features before property prediction.

## C.3 MTL and MoE

Multi-Task Learning (MTL) typically employs a shared backbone network to extract common features, followed by task-specific output heads (decoders) that specialize in individual predictions Xiao et al. (2024). In this context, the Mixture of Experts (MoE) framework offers a flexible and scalable approach to capture both shared and task-specific features by leveraging task-relevant experts. MoE has gained significant attention in multi-task scenarios across computer vision and natural language processing due to its adaptability and efficiency Riquelme et al. (2021). An MoE layer consists of a set of expert networks, denoted as  $E_i, \forall i \in [1, N]$ , where  $N$  is the number of experts, along with a routing network  $R$ . The output of an MoE layer is the weighted sum of the output  $E_n(x)$  from every expert, where weights  $G_n(x)$  are calculated by the routing network  $R$  and  $x$  represents the model input. Formally, the output of a MoE layer is given by

$$y = \sum_{i=1}^N G_n(x) E_n(x).$$

The routing network utilizes a noisy Top- $K$  selection mechanism Shazeer et al. (2017) to model the probabilities of each expert and select the top  $K$  candidates. This process is defined as:

$$G(x) = \text{TopK}(\text{Softmax}(xW + \mathcal{N}(0, 1)\text{Softplus}(xW_{\text{noise}}))),$$

where  $W$  and  $W_{\text{noise}}$  are router model parameters,  $\mathcal{N}(0, 1)$  is a standard normal distribution, and  $\text{Softmax}(\cdot)$  and  $\text{Softplus}(\cdot)$  are activation functions. Besides, the  $\text{TopK}(\cdot)$  function retains only the  $K$  largest values, setting all others to zero.

## C.4 Multi-Property Prediction Decoder

For multi-property prediction, we employ ReGNet-MT, a multi-task learning variant of ReGNet in the decoder that incorporates mixture-of-experts (MoE) layers followed by task-specific fully connected heads. We assume that the

Table 13: Comparison of MTL on The Materials Project in terms of test MAE.

Method	Formation Energy	Band Gap	Bulk Moduli	Shear Moduli
	meV/atom	eV	log(GPa)	log(GPa)
ReGNet-MT	<b>24.50</b>	<b>0.218</b>	<b>0.0391</b>	<b>0.0668</b>
ReGNet-LS	39.10	0.221	0.0404	0.0713

aggregated node features from the final ReGNet block encapsulate both short-range and long-range information of materials, which can be shared among all property prediction tasks. However, different properties require customized features before individual task heads. Therefore, experts are expected to learn distinct features, while the routing network can determine the optimal expert combination. Unlike the post-processing of the predicted property values after decoders with physical laws Ren et al. (2024), this approach offers more flexibility. Meanwhile, similar properties could have a large expert selection overlap, such that the knowledge can be shared among them. Notably, this expert-sharing mechanism could facilitate positive transfer.

### C.5 Detailed Results on Multi-Property Prediction

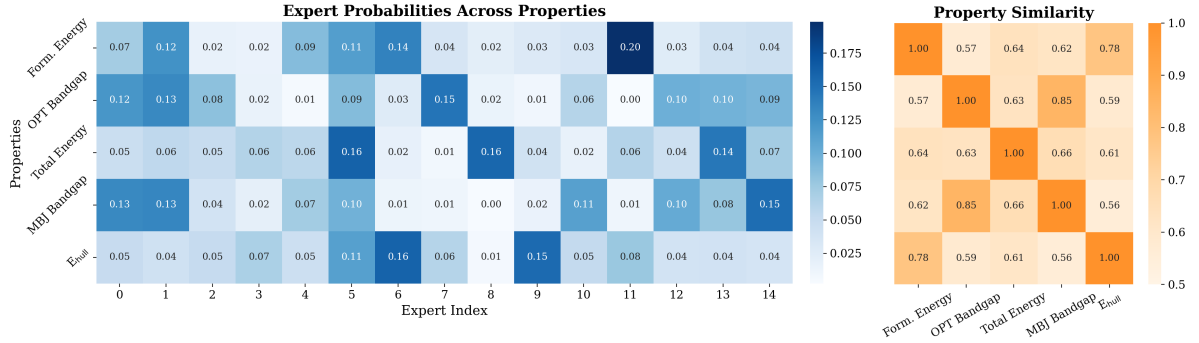


Figure 5: MoE experts frequencies for each property on the JARVIS dataset and property similarities. The expert selections in the OPT bandgap and MBJ bandgap show the highest similarity, and the positive transfer happens between these two predictions.

In this section, we provide detailed results of using ReGNet-MT on JARVIS and The Material Project datasets. We compare our method with the most accepted MTL method, linear scalarization (LS), and the results are shown in Figure 5, Table 12, and Table 13.

Performance degradation in MTL compared to STL is a well-known phenomenon in the MTL literature. This issue is commonly attributed to the gradient conflict, which arises when gradients from different tasks (properties) point in conflicting directions or have significantly different magnitudes Xiao et al. (2024). Therefore, it is realistic to expect a performance drop in both Table 12 and Table 13 for most properties, and this phenomenon becomes severe when the number of properties increases. However, our ReGNet-MT still matches Matformer and ALIGNN on both datasets.

Surprisingly, ReGNet-MT achieves the best performance for two bandgaps, though some degradation happens. Notably, bandgap (MBJ) surpasses the state-of-the-art (SOTA) results of single-task models, while bandgap (OPT) matches the SOTA performance. To evaluate this improvement, we track the selection frequencies of the 15 experts and visualize the expert selection probabilities for each task (see Figure 5, left). We also compute the cosine similarity among properties via expert selection probabilities (see Figure 5, right). Among the five tasks, two bandgap properties exhibit the highest similarity score of 0.85, indicating a big overlap in the expert selection, which facilitates the positive transfer. This finding explains why ReGNet-MT outperforms single-task training for two bandgaps.